Deep High Dynamic Range Imaging: A Case Study at S Band

W. D. Cotton January 26, 2018

***Abstract*—High dynamic range imaging of a field observed with the EVLA at S band (2-4 GHz) is discussed. The field is centered on a 200 mJy source which generated a number of artifacts. The "fingerprint" artifact which consists of many narrow curved, concentric features was caused by residual group delay errors and is eliminated by delay self calibration although the ultimate cause of the delay–like variations was not identified and warrants further investigation. The "black stripe" artifact which consists of a negative linear feature centered on the bright source is due to unflagged RFI and is removed by more aggressive flagging. However, the mechanism by which the RFI gives rise to the visible artifact is not understood. Combination of data-sets taken several weeks apart result in the "radial spoke" artifact which is presumed to be the result of brightness variation in the central source; subtracting this source before combination eliminated this artifact.**

***Index Terms*—interferometry, dynamic range**

I. Introduction

AT low radio frequencies the sky is filled with bright sources. The artifacts generated by these sources can limit the depth to which a given field can be imaged. This memo discusses a test case observed at S band by the EVLA and reduced using the Obit package [1] [1]. Several dynamic range limiting artifacts are encountered, analyzed and removed.

II. Limits to Dynamic Range

There are a number of effects which can limit the dynamic range of images at low radio frequencies. One important category is calibration. Amplitude and/or phase errors will distort the images of the brighter emission, scattering power across the field. Self calibration can greatly reduce these effects.

Errors in the group delay (slope of phase with frequency) calibration can produce artifacts in CLEANing as it introduces frequency dependent phase errors. When the Fourier transform of the sky model is subtracted from the data, systematic errors will remain which can produce visible artifacts. Self calibration determining delay errors can correct such errors. This effect will be considered further in the following.

There are a variety of direction dependent effects such as the amplitude variations caused by the rotation of asymetries in antenna patterns with parallactic angle or phase variations due to irregularities in the ionospheric phase screen. Uncorrected variation of antenna gain [2], [3] in the direction of bright sources will make them appear to be variable leaving artifacts which are not convolutional. Phase errors can shift and distort sources [4] in a time variable fashion. "Peeling", localized gain solutions [5], can reduce these artifacts.

Representations of the sky as values on a rectangular grid of pixels is an approximation which may have difficulty in representating the true, continious sky brightness. Bright unresolved sources not exactly located on a pixel are problematic [6]. It is possible to approximate such sources with an infinite series of positive and negative CLEAN components but in practice this leads to artifacts around bright sources. For a single source the imaging grid can be adjusted to center the source on a pixel. For the general case of multiple bright sources, faceted imaging [7], [6] allows an arbitrary number of sources to be centered on a pixel.

For wide-band images, an accurate representation of the spectrum of the sky model is critical. Such datasets contain many frequency channels to avoid bandwidth smearing and the sky model must be accurately intrepreted in a frequency dependent fashion when subtracting it from the residual data or when used in self calibration.

Polarization impurities in the interferometer feeds and antenna patterns [8],[9],[2] can introduce higher order corruptions of the signals which will result in imaging artifacts. Calibration of the polarization state of the instrument may be needed to eliminate such artifacts.

Variations in the flux densities of strong sources are possible in data-sets obtained over an extended period. As for uncorrected antenna gain variations, the variable brightness of the source will result in artifacts which are not convolutional and are not removed by deconvolution.

Very strong interference (RFI) can reduce the gain of the interferometer electronics with variations on short time scale; this can affect data outside of the range of frequencies at which the troublesome signals occur. With the EVLA, the "switched power" calibration can largely remove these effects. Amplitude self calibration can also help.

Residual RFI in the data can increase the noise as well as introduce visible artifacts; these are independent of any emission in the field. Furthermore, RFI can modify the effective interferometer response to a strong source; this is especially troublesome given that it is more difficult to detect RFI in data including strong sources. This effect can introduce artifacts around these brighter sources as is shown in the following.

III. EVLA S Band Case

The data discussed in this memo were part of a project observing a northerly field with the EVLA in S band (2-4 GHz)

National Radio Astronomy Observatory, 520 Edgemont Rd., Charlottesville, VA, 22903 USA email: bcotton@nrao.edu

[1] http://www.cv.nrao.edu/∼bcotton/Obit.html

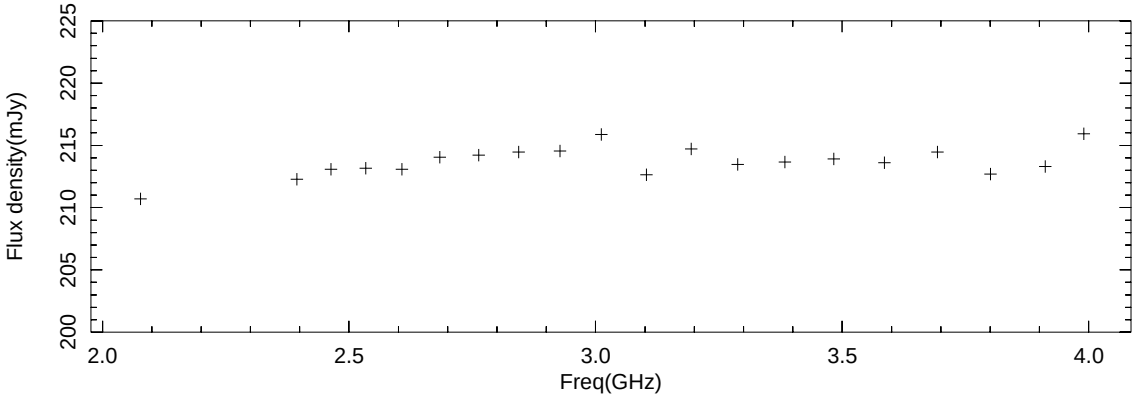

Fig. 1. Central source spectrum from one session's image.

using the "B" configuration (resolution ≈2.5"). Two sessions of two hours each were obtained. The field is centered on a 200 mJy point source which has the potential to limit the dynamic of the eventual sub-μJy image. The central source has a flattish spectrum but appears to peak in the observed band-pass; see Figure 1.

A. Initial Calibration and Editing

The data were calibrated and edited using the standard Obit EVLA calibration scripts [10]. This procedure used the "switched power" measurements which should correct for gain fluctuations due to the variable RFI environment. The first data-set used 3C48 as the flux density calibrator which, while resolved, with the use of the standard model was adequate for this observation. The second session used 3C295 which was too resolved, even with the model, to give adequate calibration. The spectrum for the phase reference calibrator, common to both, derived for the first observation was used in the second.

Calibration and editing are intermixed and the calibration steps consisted of:

1) Switched power calibration.
2) Delay calibration using the phase reference source.
3) Band-pass calibration using the amplitude calibrator and calibrator model.
4) Amplitude and phase calibration using the amplitude calibrator and model to determine the spectrum of the phase reference calibrator.

Due to the limited parallactic angle coverage of the data-sets, no polarization calibration was determined.

Data editing of the target field at this stage consisted of running median windows in time and frequency looking for outlyers. The efficacy of this depends on there being enough good data at given times and frequencies to distinguish the bad; this is not always the case. Calibrators were subjected to additional editing including that based on searching for outlyers in various calibration solutions.

Once a pass was made through calibrating and editing, the calibration tables were discarded, the flag table kept and the process repeated. This process results in calibration largely free of the corruptions from RFI. The target field data described here had visibilities with amplitudes in excess of 0.35 Jy flagged.

B. Initial imaging

Following the external calibration, each data-set was imaged using phase only followed by amplitude and phase self calibration. Imaging used Obit wide-band, wide-field imager MFImage. This program independently constructs dirty/residual images in a set of frequency bins and does a joint deconvolution. The result is an image cube with coarse frequency resolution. The spectrum of the sky model is represented by a table of the flux densities in each of the frequency bins in each CLEAN component [11]. In evaluating the CLEAN component to determine the sky model using the "DFT" technique, the frequency bin tabulated values are extrapolated in frequency using a spectral index fitted to the spectrum in each component. The field being imaged was centered on a bright, unresolved source and self calibration accurately centered it on a pixel at the center of the central facet.

The central portion of the field imaged from one session is shown in Figure 2. Several artifacts related to the bright source in the center are apparent. First is the "fingerprint" pattern of narrow, curved features. The second is the horizontal dark bar ("black stripe") centered on the bright source and fainter but wider dark bands below and above the central source.

C. Residual delay errors

In order to help identify the source of the fingerprint artifacts, all emission other than the central source was subtracted from the data and all visibilities on all baselines and at all times were averaged into a single visibility spectrum. This visibility is plotted in Figure 3. Other than the reduced amplitude at the ends of each spectral window, the only curiosites are the small ramps of phase with frequency in each spectral window. This is the signature of a residual group delay error.

These data were delay calibrated using the scans on the phase reference calibrator interpolated to the times of the target field data which should remove any slowly varying delay errors

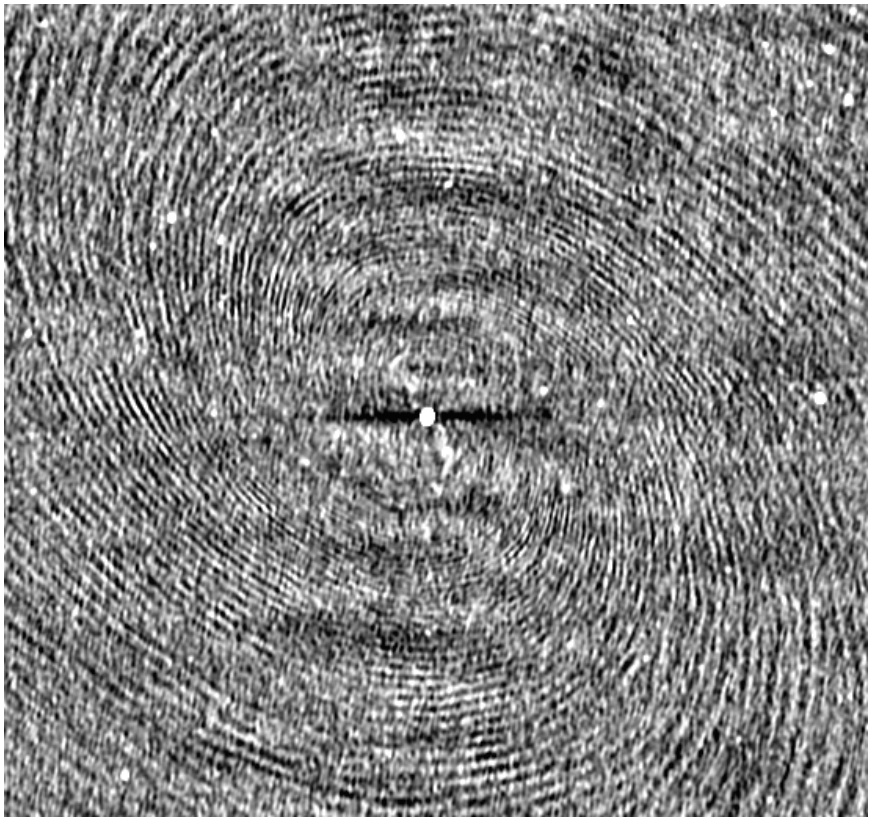

Fig. 2. Image from one session showing "fingerprint" and "black stripe" artifacts. Negative gray-scale with $\pm 20\mu$Jy/beam. Region shown is 9.2' $\times$ 8.7'.

common to the two adjacent fields. The central source is strong enough that residual delay errors can be determined on a short time scale. Some of the results of such a fitting are shown in Figures 4–6. Figure 4 shows residual delays as a function of time for a number of spectral windows and both polarizations for an antenna for which these values were well behaved, flat and scattered around zero. Figure 5 shows a less well behaved case with time varying mean delays. These non–zero features are centered on the calibrator scan at 1:10. The calibrator data in question is well behaved and the solutions well describe the data, just with a different delay than at other times. These features will contribute to the residual delays seen in Figure 3. Figure 6 shows fitted delays for the innermost antenna on one arm in which the quantized delay update required for a digital interferometer are very visible. For antennas further from the center of the array, these updates happen too often to be resolved by the solution interval used. The delay variations due to the quantized interferometer delay updates are unlikely to give rise to the visible artifacts as they are too rapid and are centered on zero delay and should average out.

Removing the fitted group delay errors in the target field resulted in data-sets whose images had no signs of the fingerprint artifact. This artifact is therefore the result of small but systematic, residual delay errors. Obit imaging tasks have phase and delay fitting as an option in self calibration.

D. Source Subtraction

The delay corrected data-sets were combined and imaged with self calibration resulting the Figure 7. The prominent "radial spokes" are likely due to variations in the brightness of the central source in the several weeks between the two observing session and do not appear in either data-set independently. The peaks in the two individual images are 213.7 and 199.5 mJy although this difference could be due to the calibration. However, the amplitude self calibration used in deriving Figure 8 should have removed a simple difference in the amplitude calibration.

In order to test this hypothesis, the central source from the derived image was subtracted from each self calibrated data-set and then the data were combined and imaged without further self calibration resulting in Figure 8.

E. Deeper RFI flagging

Figure 8 shows that the fingerprint and radial artifacts have been removed. The remaining artifacts are the dark band through the central source and the fainter bands above and below. Obit imager MFImage produces an image cube with some spectral resolution allowing the determination that these artifacts largely appear in the spectral windows at the top of the observed band where strong RFI is know to occur. Time series flux densities of spectral window averaged data on individual baselines show periods of unremoved RFI; an example is shown in Figure 9. The visibility spectrum of the same baseline averaged over the period of the peak RFI seen in Figure 9 is shown in Figure 10.

After the subtraction of the central source only a few mJy of flux density remains in the data-set so aggressive clipping is possible. After averaging to 2 min, flagging to remove

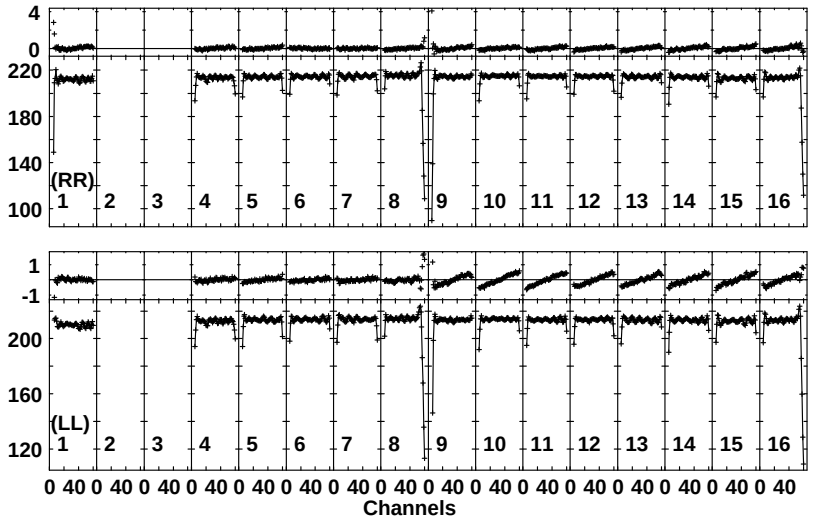

Fig. 3. Spectrum of averaged data-set showing delay errors. Amplitudes shown in lower panels in mJy and phases in the upper panels in degrees.

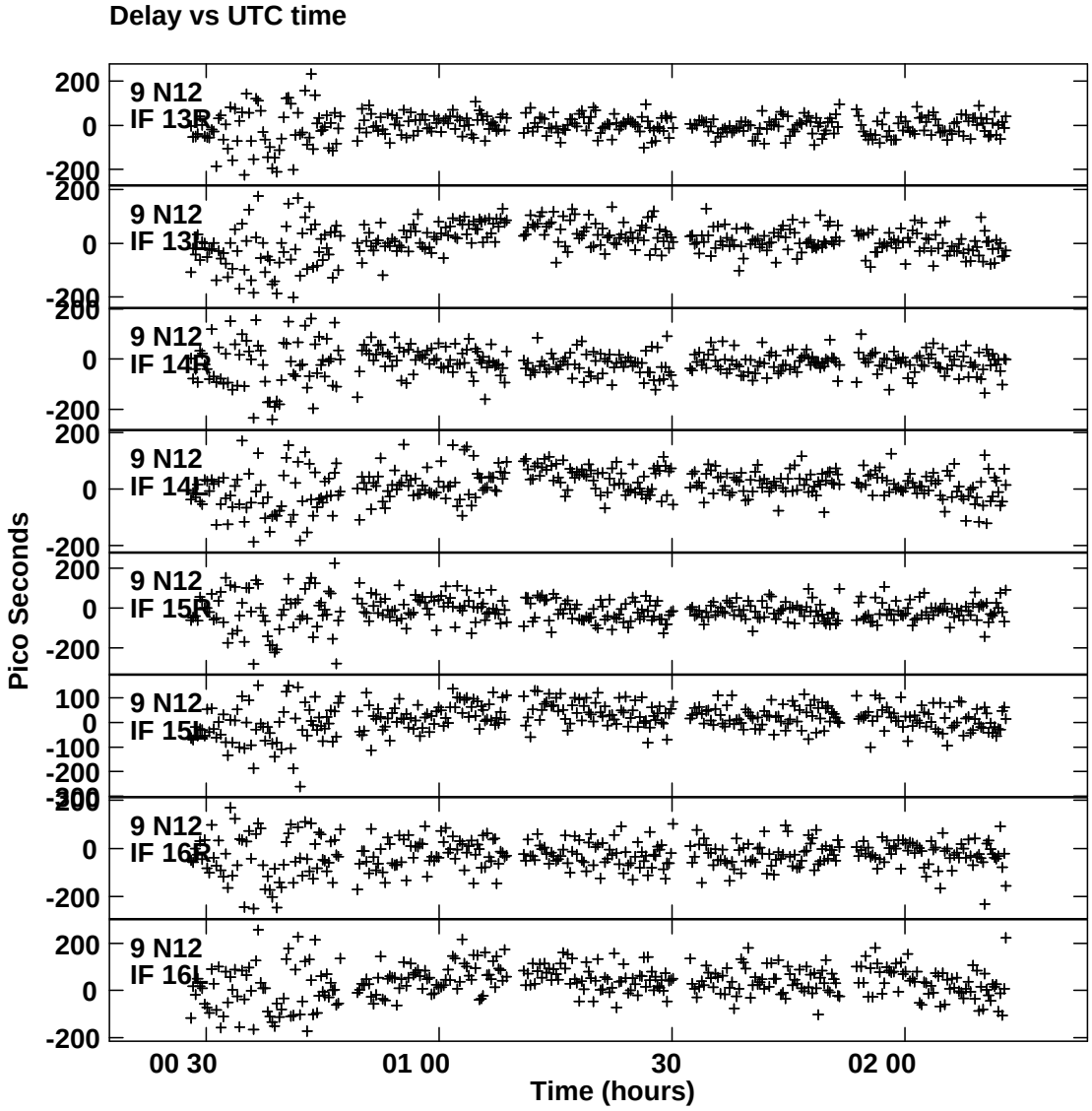

Fig. 4. Fitted residual delay on the target field versus time for a number of spectral windows and RCP/LCP for relatively well behaved data. The gaps were for calibrator observations

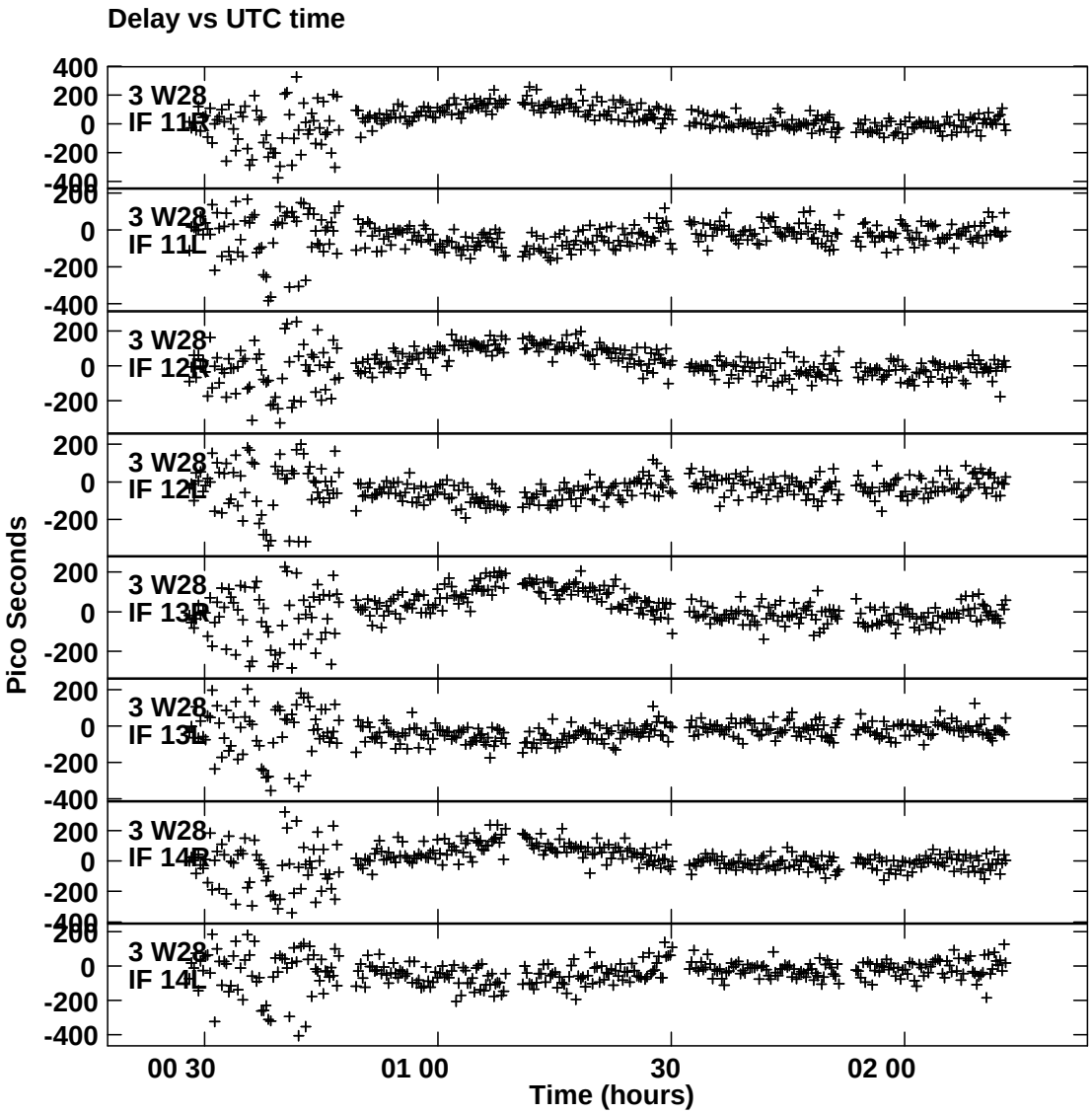

Fig. 5. Like Figure 4 but for spectral windows and polarizations which are not well behaved. In particular, the calibrator measurements at 1:10 cause the bends in the curves.

visibilities with amplitudes above 35 mJy was determined and applied to the data. The resulting data were imaged producing Figure 11. This image has almost all of the visible artifacts removed. The off-source RMS is 3.2 μJy/beam giving a dynamic range of 65,000:1 and a basically noise limited image.

IV. Discussion

Some potential sources of dynamic range limiting image artifacts are reduced by the general techniques used in Obit imaging. These include accurate intrepretation of the frequency dependence of the sky model and the centering of the bright central source on a pixel. However, the previous sections have demonstrated several other strong source artifacts remaining. Additional techniques to suppress them were described. These are discussed further below.

The "fingerprint" artifact (Fig 2) was traced to systematic errors in the group delay calibration. These are easily dealt with using delay self calibration but the fundamental cause of the problem is less clear. The delays fitted describe the reality of the data in the sense that when applied, the phases become quite flat in time and frequency. The variations in fitted delay do not all appear to be related to variations in atmospheric or ionospheric delay variations (e.g. have different behavior in RCP and LCP and differences among antennas) and may be due to RFI making minor frequency dependent modification of the observed phases.

The "radial spoke" artifact seen when the two observations separated in time by several weeks are added is likely due to variations in the flux density of the central source. The spectrum of this source suggests that it is physically very small and variations on short time scales are possible. Subtracting the response of the central source from each data-set after self calibration appears to have removed the problem and may be the general solution to this problem.

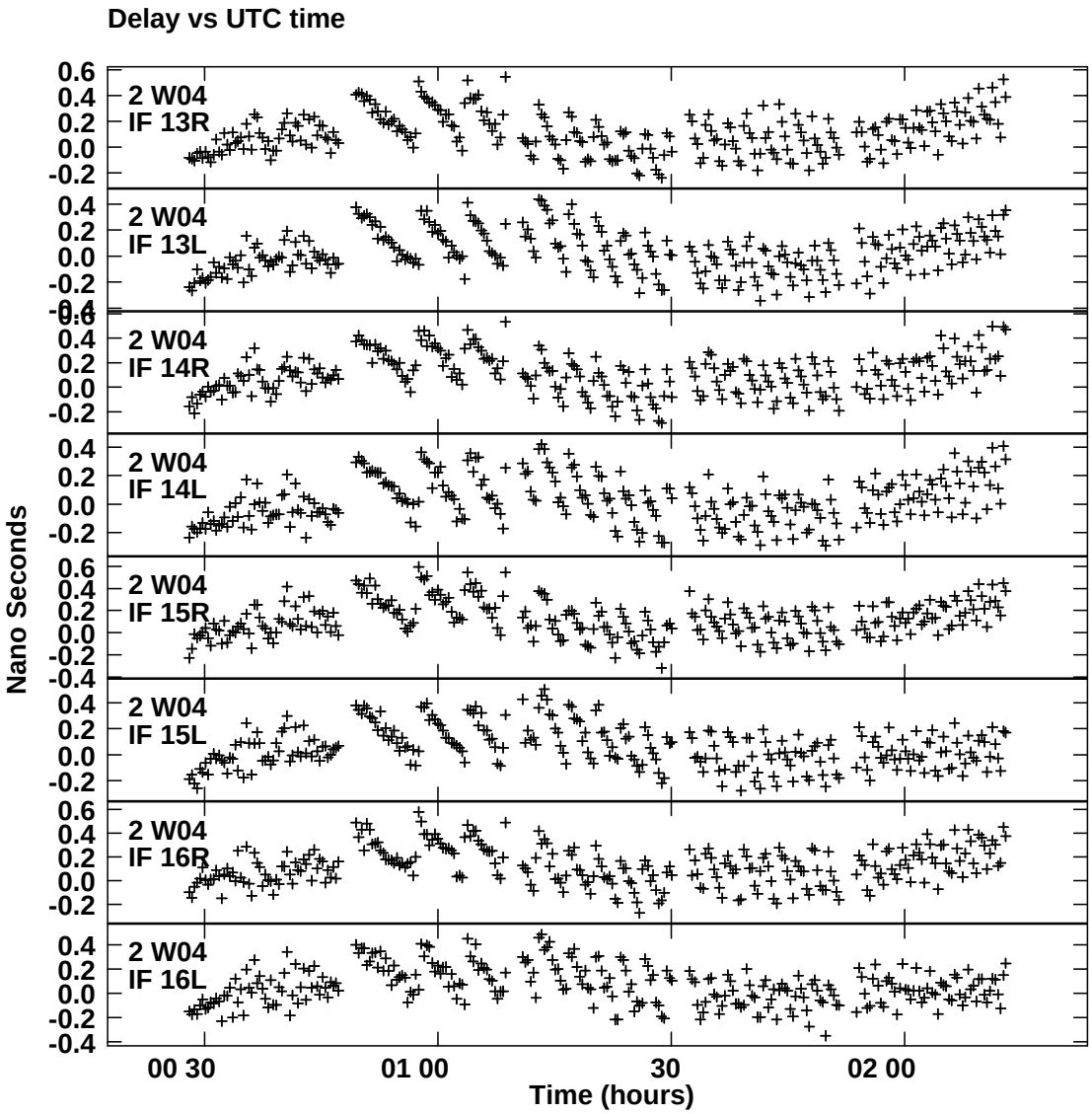

Fig. 6. Like Figure 4 but for the inner antenna on the west arm showing the effects of the delay updates of the interferometer.

The "black stripe" artifact was traced to unflagged RFI which modified the image of the central source. After the central source was subtracted only about 10 mJy of flux density remained and very aggressive clipping of the time averaged data was possible. A more general solution is to subtract the full CLEAN sky model of the field from the data, average in time and/or frequency to form a data-set on which a sensitive search for RFI can be performed. The mechanism by which RFI produces the observed artifact is unclear.

The final image of the data examined here only had a dynamic range of 65,000:1 but was largely noise limited and deeper observations would be feasible.

ACKNOWLEDGMENT

I wold like to thank Jim Condon, Oleg Smirnov and Rick Perley for thoughtful comments.

REFERENCES

[1] W. D. Cotton, "Obit: A Development Environment for Astronomical Algorithms," *PASP*, vol. 120, pp. 439–448, 2008.

[2] W. D. Cotton and R. Perley, "EVLA Off-axis Beam and Instrumental Polarization," *Obit Development Memo Series*, vol. 17, pp. 1–22, 2010. [Online]. Available: ftp://ftp.cv.nrao.edu/NRAO-staff/bcotton/Obit/EVLABeam.pdf

[3] ——, "EVLA Beam Holography take 2," *Obit Development Memo Series*, vol. 47, pp. 1–13, 2017. [Online]. Available: ftp://ftp.cv.nrao.edu/NRAO-staff/bcotton/Obit/EVLABeam17.pdf

[4] W. D. Cotton and J. Uson, "Ionospheric Effects and Imaging and Calibration of VLA Data," *EVLA Memo Series*, vol. 118, pp. 1–12, 2007.

[5] W. D. Cotton, "Manual Peeling in Obit," *Obit Development Memo Series*, vol. 54, pp. 1–5, 2017. [Online]. Available: ftp://ftp.cv.nrao.edu/NRAO-staff/bcotton/Obit/ManPeel.pdf

[6] W. D. Cotton and J. Uson, "Pixelization and Dynamic Range in Radio Interferometry," *A&A*, vol. 490, pp. 455–460, 2008.

[7] W. D. Cotton and W. L. Peters, "Tiling the Field of View with Facets," *Obit Development Memo Series*, vol. 42, pp. 1–2, 2016. [Online]. Available: ftp://ftp.cv.nrao.edu/NRAO-staff/bcotton/Obit/TileFOV.pdf

[8] W. D. Cotton, "On–axis Instrumental Polarization Calibration for Circular Feeds," *Obit Development Memo Series*, vol. 30,

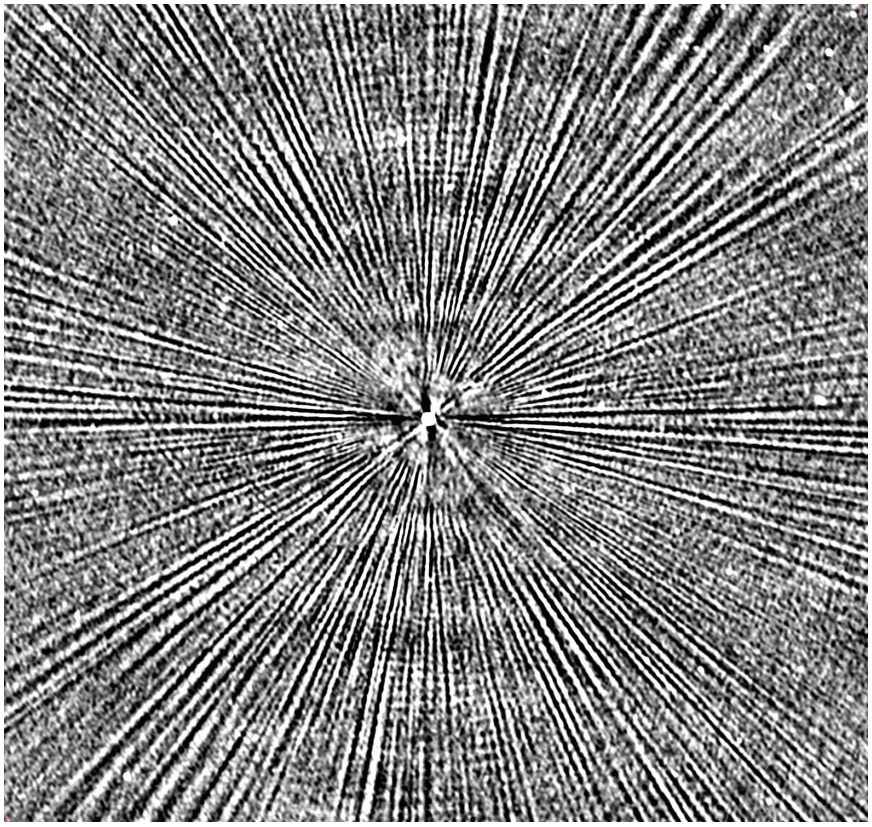

Fig. 7. Combined data-set image without subtracting the central source showing the “radial spokes” artifacts. Negative gray-scale with $\pm 10 \mu$Jy/beam. Region shown is 9.2’ $\times$ 8.7’.

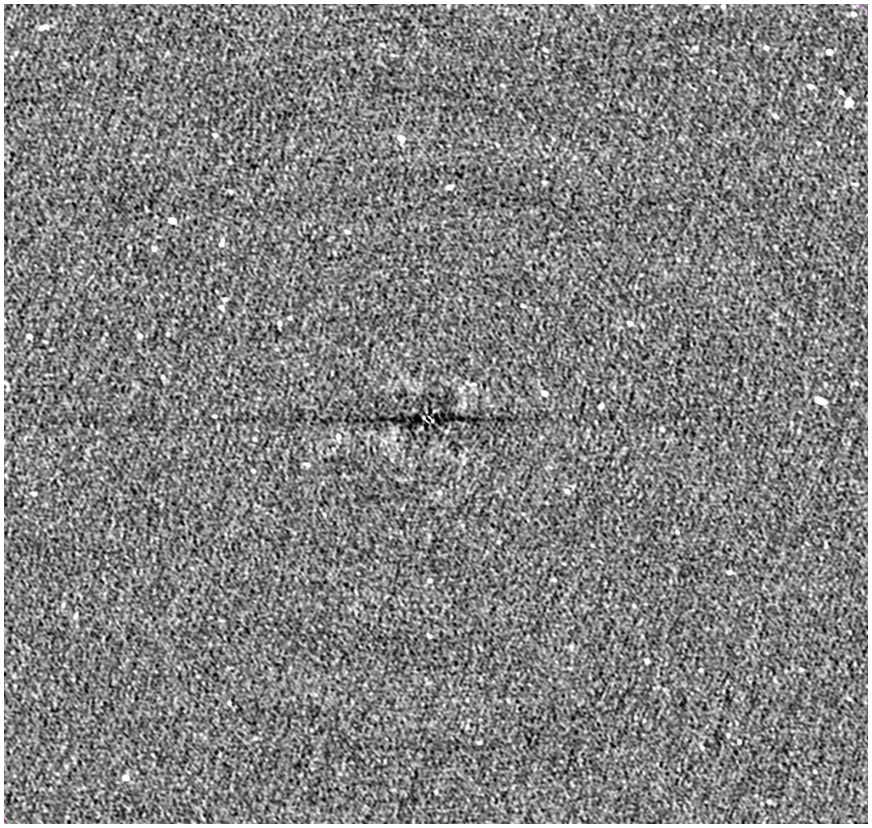

Fig. 8. Combined data-set image after subtracting the central source, “black stripe” artifact remains . Negative gray-scale with $\pm 10 \mu$Jy/beam. Region shown is 9.2’ $\times$ 8.7’.

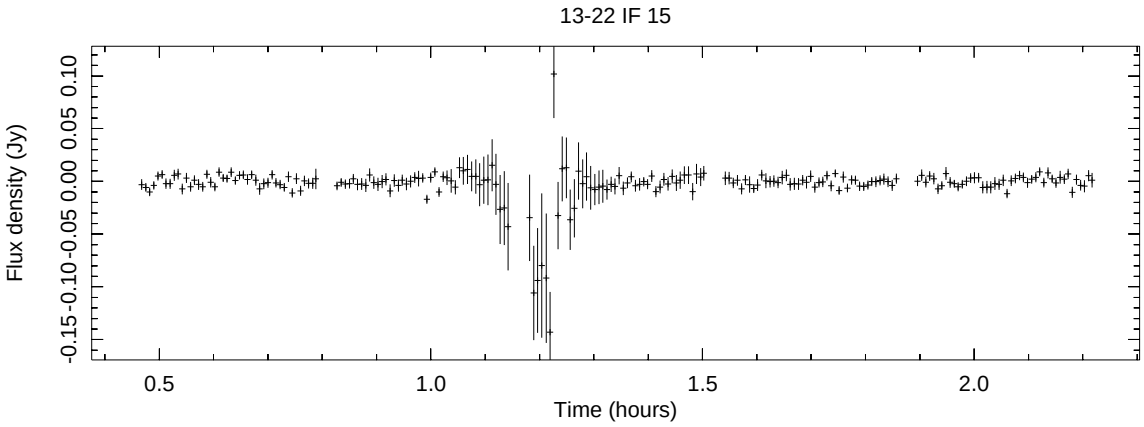

Fig. 9. Frequency averaged real part of the visibility of baseline 13-22 in spectral window 15 versus time. The central source has been subtracted.

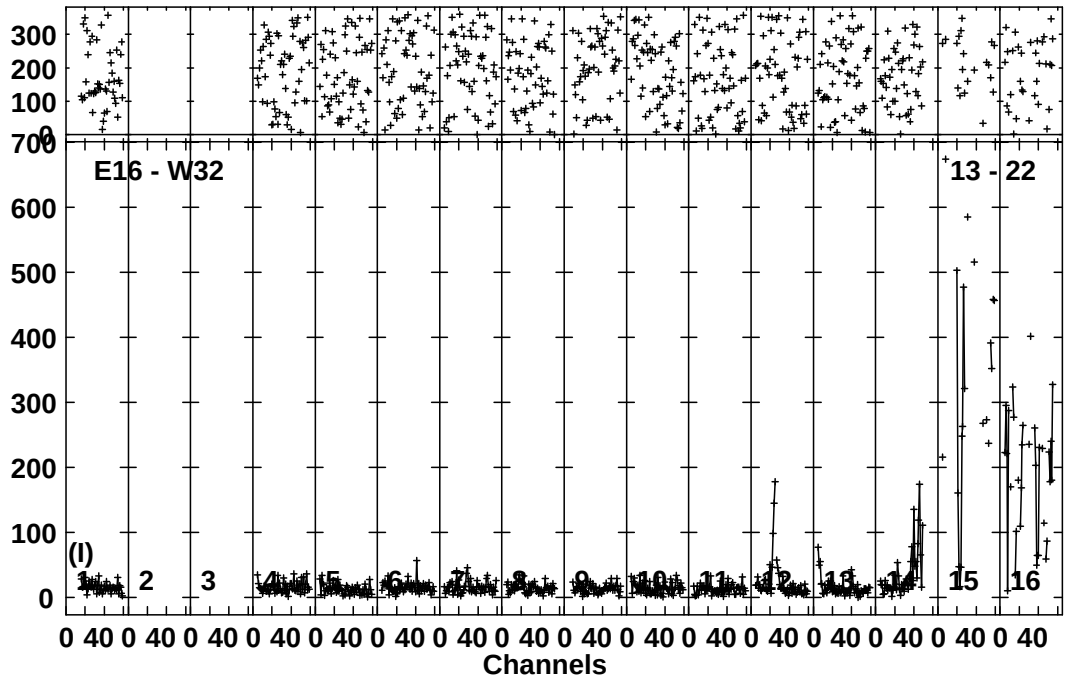

Fig. 10. Visibility spectrum of baseline 13-22 during minimum seen in Figure 9. Amplitudes shown in lower panels in mJy and phases in the upper panels in degrees. Note: much of the data in spectral windows 15 and 16 were flagged in the calibration process. All of spectral windows 2 and 3 are lost to RFI.

p. 14, 2012. [Online]. Available: ftp://ftp.cv.nrao.edu/NRAO-staff/bcotton/Obit/PCalRL.pdf

[9] ——, "On–axis Instrumental Polarization Calibration for Linear Feeds," *Obit Development Memo Series*, vol. 32, p. 11, 2015. [Online]. Available: ftp://ftp.cv.nrao.edu/NRAO-staff/bcotton/Obit/PCalXY.pdf

[10] ——, "EVLA Continuum Scripts: Outline of Data Reduction and Heuristics," *Obit Development Memo Series*, vol. 29, pp. 1–25, 2012.

[11] ——, "Interferometry Wideband, Widefield Calibrator Models," *Obit Development Memo Series*, vol. 38, pp. 1–6, 2014. [Online]. Available: ftp://ftp.cv.nrao.edu/NRAO-staff/bcotton/Obit/CalModel.pdf

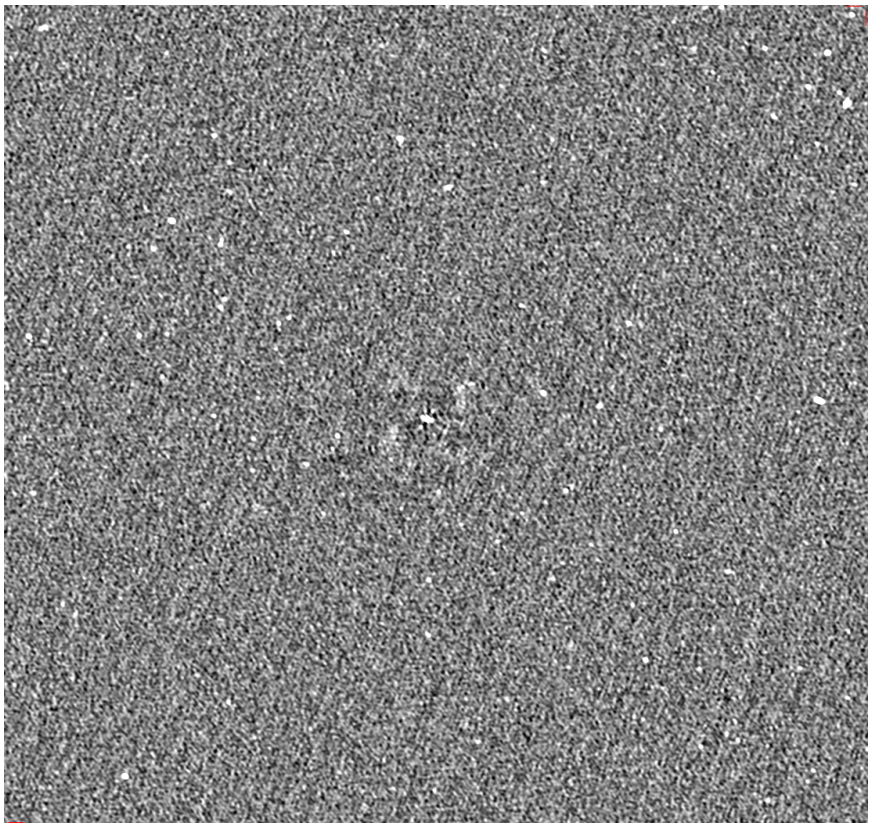

Fig. 11. Combined, subtracted data-set image after deeper RFI flagging. Negative gray-scale with $\pm 10\mu$Jy/beam. Region shown is 9.2' $\times$ 8.7'. RMS is 3.2μJy/beam.